Ultramicroscopy 109 (2009) 1148–1156

Contents lists available at ScienceDirect

Ultramicroscopy

journal homepage: www.elsevier.com/locate/ultramic

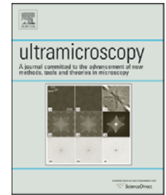

Bragg's Law diffraction simulations for electron backscatter diffraction analysis

Josh Kacher *, Colin Landon, Brent L. Adams, David Fullwood

Department of Mechanical Engineering, Brigham Young University, 455B Crabtree Technology Building, Provo, UT 84602, USA

ARTICLE INFO

Article history:
Received 15 January 2009
Received in revised form
3 April 2009
Accepted 28 April 2009

PACS:
87.64.Bx
61.72.Hh

Keywords:
Scanning electron microscope
Dislocations
EBSD
Strain

ABSTRACT

In 2006, Angus Wilkinson introduced a cross-correlation-based electron backscatter diffraction (EBSD) texture analysis system capable of measuring lattice rotations and elastic strains to high resolution. A variation of the cross-correlation method is introduced using Bragg's Law-based simulated EBSD patterns as strain free reference patterns that facilitates the use of the cross-correlation method with polycrystalline materials. The lattice state is found by comparing simulated patterns to collected patterns at a number of regions on the pattern using the cross-correlation function and calculating the deformation from the measured shifts of each region. A new pattern can be simulated at the deformed state, and the process can be iterated a number of times to converge on the absolute lattice state. By analyzing an iteratively rotated single crystal silicon sample and recovering the rotation, this method is shown to have an angular resolution of ~0.04° and an elastic strain resolution of ~7e−4. As an example of applications, elastic strain and curvature measurements are used to estimate the dislocation density in a single grain of a compressed polycrystalline Mg-based AZ91 alloy.

© 2009 Elsevier B.V. All rights reserved.

1. Introduction

Orientation imaging microscopy (OIM), an electron backscatter diffraction (EBSD)-based texture analysis system, has been a key tool in the study and characterization of polycrystalline materials. OIM uses a Hough transform to identify bands in EBSD patterns, and then uses a lookup table to identify these bands and determine the crystal lattice orientation. Statistically significant datasets on the crystal orientation of a material can be collected in relatively short amounts of time. A number of limitations of OIM, however, have motivated the continued search for a more robust system of EBSD-based texture analysis. A new EBSD-based texture analysis system that relies on simulated EBSD patterns and the cross-correlation function is presented in this paper. This new system addresses two of the main limitations of OIM; specifically its angular resolution (~0.5° misorientation [1,2]) and its insensitivity to elastic strain.

A cross-correlation-based orientation and strain measurement system introduced by Troost et al. [3] and refined by Wilkinson et al. [4,5] has been shown to achieve orientation resolution to 0.006° and measures all nine components of the elastic deformation gradient tensor to 1×10^{-4}. This new method, however, is confined to measuring elastic strain and lattice orientation gradients except in the case when a strain-free reference EBSD pattern is available. In practice, such patterns exist only in limited situations. Instead, EBSD patterns can be simulated at known reference states, thus eliminating the ambiguity associated with an experimentally collected pattern. The absolute strain and rotation of a measured pattern can then be calculated by comparison to a pattern simulated for a known lattice state. Because high-fidelity simulations are computationally costly, simple Bragg's Law-based patterns were investigated for use as reference patterns. There are two fundamental questions upon which the feasibility of using Bragg's Law based simulations as reference patterns hang. First, will the cross-correlation analysis of a measured pattern with a simulated one return appropriate shifts, and second, are kinematical simulations sufficiently accurate to make meaningful measurements. This study shows that by iteratively generating the simple patterns at each calculated deformation state of a measured pattern and then repeating the calculation with the new simulation, a high-resolution result—approaching the levels of the standard cross-correlation based method—is rapidly found by convergence. In this way, the benefits of the cross-correlation method are kept while the limitations associated with needing a strain-free reference pattern are eliminated. As an example application, the simulated pattern method has been applied to estimating the dislocation density for a compressed magnesium alloy sample.

* Corresponding author. Tel.: +1 952 594 4531.
E-mail address: jkacherbyu@gmail.com (J. Kacher).

0304-3991/$ - see front matter © 2009 Elsevier B.V. All rights reserved.
doi:10.1016/j.ultramic.2009.04.007

2. Cross-correlation analysis of EBSD patterns

2.1. Experimental facilities

The electron backscatter data used for the single crystal silicon portion of this study was collected on a Phillips XL30 S-FEG microscope equipped with a phosphor screen detector and CCD camera. Pattern collection was controlled by the TSL OIM DC 4.6 software, and the images were collected and stored at the resolution of 1000×1000 pixels in the Tiff format. The data for the magnesium alloy sample was collected on an FEI dual beamed FIB/SEM system equipped with a Hikari high speed camera. The patterns were collected and stored at the resolution of 465×465 pixels in the bitmap format. Analysis of the patterns was then performed offline using a MATLAB code written by the authors.

2.2. Cross-correlation analysis algorithm

The approach developed by Troost and Wilkinson forms the underpinnings of the simulated pattern method to be introduced, so its fundamentals are briefly described.

Many regions of interest (ROIs) (normally 10–20) are spread uniformly around a reference EBSD pattern (see Fig. 2 for visualization). For a 1000×1000 pixel image, these regions are usually selected to be of size 256×256 pixels. Ideally, the orientation and lattice strain of the reference pattern are known. In reality the lattice state can be known only to the precision of traditional methods informed by knowledge of the material in question. ROIs in corresponding positions are placed in a different collected pattern of unknown character. The cross-correlation is then used to determine how the corresponding ROIs in the two patterns would need to be shifted in order to align similar features with each other. The cross-correlations are essentially the convolution of two functions and can be calculated efficiently in the Fourier domain by the following equation. ($\Im\{\ldots\}$ indicates the Fourier transform, $conj(\ldots)$ the complex conjugate, and * indicates element-wise multiplication of two matrices)

$$C = \Im^{-1}\{\Im\{f\} * conj(\Im\{g\})\} \tag{1}$$

The resulting image, C, shows intensity peaks related to shifts that cause similar features to be aligned. The peak intensity in the cross-correlation image, C, is located at a position described by the vector $\vec{q}$ measured from the center of the image (i.e. if the peak appears at the center then $\vec{q}$ would have components [0,0], if the peak appears one pixel to the right of and one pixel down from the center then q would have components $[-1,1]$). The vector $\vec{q}$ describes how (on average over the ROI) features contained in the selected ROI shift when compared to other patterns that also contain the feature. Local interpolation schemes over a number of ROIs allow the tracking of a feature shift down to 1/20th of a pixel. Although this shift is the average of all features in the region, it approximates the shift of the pattern direction, $\hat{r}$, found at the center of the ROI. The schematic given in Fig. 1 illustrates the connection between crystal lattice deformation and a shift in the EBSD pattern as measured on the phosphor screen. The following geometrical relation is similar to that proposed by Wilkinson et al. but has been modified to more precisely represent the actual deformation geometry

$$\frac{\vec{q}}{\lambda} = \vec{w} - (\vec{w}\cdot\hat{r}')\hat{r}' + \frac{\vec{q}\cdot\hat{r}'}{\lambda}\hat{r}' \tag{2}$$

Here $\vec{q}$ is the shift in the EBSD patterns as measured on the phosphor, $\hat{r}$ is the unit vector pointing from the specimen origin to the ROI center on the phosphor screen, and $\hat{r}'$ points to the shifted position of the ROI in the deformed lattice pattern. λ is a geometrical factor and is given by $\lambda = z^*/\hat{r}^{pc}\cdot\hat{r}$, where $\hat{r}^{pc}$ is a unit vector normal to the phosphor screen that passes through the sample origin and z^* is the perpendicular distance from the screen to the sample origin. The displacement under deformation is represented by the vector $\vec{w}$, where $\vec{w} = A\hat{r}$. A is the displacement gradient tensor, $(A+I) = F$, and F is the local deformation gradient tensor (its dependence upon location in the sample frame is implicit).

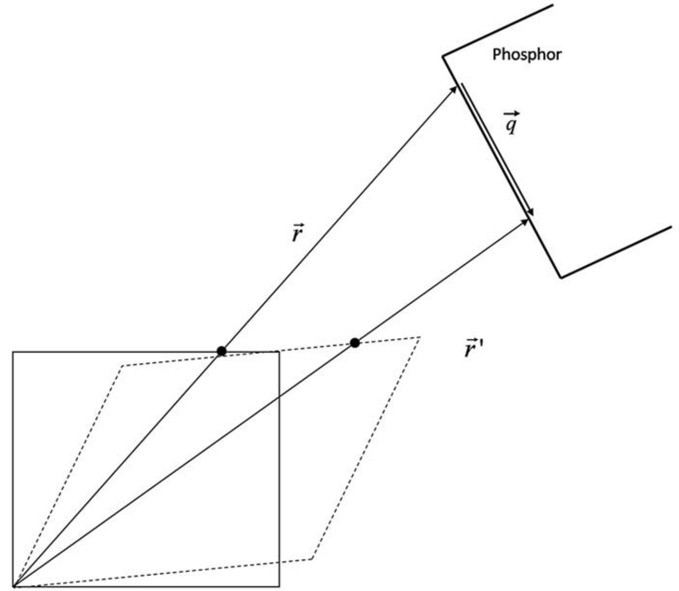

Fig. 1. Schematic of how a strain and a rotation in the crystal lattice (greatly exaggerated) can be related to a shift of an EBSD pattern on the phosphor screen. The strained lattice is represented by the dashed line.

Eq. (2) contains three independent equations, one for each component of $\vec{q}$ (the third component of $\vec{q}$ is uniformly zero when described in the coordinate frame of the phosphor screen, but is non-zero in other coordinate frames). Knowing the configuration of the microscope geometry and the appropriate coordinate frame transformations, $\hat{r}$ is easily calculated for any ROI. Using the measured shifts $\vec{q}$, $\hat{r}'$ can also be evaluated. This leaves the displacement gradient tensor as the only unknown. In addition to the three independent equations from the components of the above relationship, three more equations can be added from the appropriate form of the traction-free boundary condition for the sample surface with unit normal $\hat{r}^{pc}$ either in terms of stress, σ, or elastic stiffness, C, times strain, ε

$$0 = \sigma_{ij}\,\hat{r}_j^{pc} = C_{ijkl}\varepsilon_{kl}\hat{r}_j^{pc} \tag{3}$$

For small deformations, the symmetric and asymmetric parts of the displacement gradient tensor A represent, respectively, the elastic strain and rotation according to the following equations:

$$\varepsilon = \tfrac{1}{2}(A + A^T) \text{ and } \omega = \tfrac{1}{2}(A - A^T) \tag{4}$$

The reader is reminded that the polar decomposition theorem enables the deformation gradient tensor, F, to be expressed as the product of a proper orthogonal tensor or rotation, R, and a positive definite symmetric tensor, U: $F = RU$. In the case of the small elastic deformations and rotations of the crystal lattice, ω can be related to the rotation tensor by $R = I+\omega$, and ε is related by the expression $U = I+\varepsilon$.

Care must be taken to express all terms in the above equations in the same reference frame—usually the deformed (or sample) frame or the reference (or crystal) frame. However, difficulties with the boundary condition are that, first the elastic constants must be known, second the appropriate deformation must be

known to express the elastic stiffness tensor, C, in the deformed frame. Conversely the appropriate deformation must be known to express $\hat{r}^{pc}$ in the crystal frame, but until the boundary condition equations are evaluated, the deformation is not completely known. This circular dependence may be resolved by an iterative process where an initial assumption is made about deformation, and then the calculated deformations are used to update subsequent iterations. This approach is described in detail later. The system composed of Eqs. (2) and (3) may be solved by choosing only two ROIs. (Note that this is a decrease in the number of requisite ROIs from Wilkinson's method because the system of equations includes the boundary conditions rather than imposing them after evaluation of the deformation geometry equation. However, this reduction is of no technical significance because typically 10–20 ROIs are chosen to reduce the effects of noise and improve resolution.)

A new error measure was defined to describe the fit of a calculated deformation tensor to the shifts measured on the phosphor screen. To evaluate the fit, the shifts that would have been caused by a measured deformation tensor, F, are calculated, and then the average length of the difference between the calculated and measured shifts is found. For N ROIs in an EBSD pattern the error measure is defined as follows where ${}^{i}\hat{r}$ is the direction of the center of the ith ROI, ${}^{i}\vec{q}^{m}$ and ${}^{i}\vec{q}^{c}$, are the measured and calculated shifts of the ith ROI, P is the plane that contains the phosphor screen and $\bar{e}$ is the average error for all N ROIs

$$ {}^{i}\vec{q}^{c} = {}^{i}\hat{r} - (F\,{}^{i}\hat{r}) \bigcap P \tag{5} $$

$$ \bar{e} = \frac{1}{N} \sum_{i=1}^{N} |{}^{i}\vec{q}^{c} - {}^{i}\vec{q}^{m}| \tag{6} $$

The $|\ldots|$ notation in Eq. (6) denotes the scalar magnitude, and $\cap$ in Eq. (5) denotes the intersection of sets. The error measure $\bar{e}$ describes how well the calculated F fits the measured shifts.

2.3. Variables and limitations

Despite the enhancements of cross-correlation-based analysis over the traditional Hough transform method, there are a few inherent hurdles that instigated the search for algorithm improvements. The quality of EBSD images has always been a major factor in OIM, and when trying to extract sub-pixel level information from the patterns, pattern quality becomes even more of an issue. Various filtering tools and techniques are essential to obtain any meaningful results from the analysis, and the filter adjustments are not easily automated. The two most detrimental features that must be filtered are non-uniform intensity of the EBSD pattern background, caused by the electron probe creating a bright spot on the phosphor screen in the area of highest incident electron density, and dark spots in the pattern image resulting from defects on the phosphor screen [6]. There exist several standard techniques for dealing with these issues, including normalized cross-correlations [7], various filtering techniques [8], and the use of features standard to most EBSD systems such as TSL-OIM's background subtract feature [9]. These defects continue to play a role in pattern-to-pattern comparisons. The main obstacle in the general application of cross-correlation-based methods, however, is their reliance on a reference pattern.

3. Bragg's Law pattern simulations

Dependence on a reference pattern allows for measurements of elastic strain and orientation gradients, but makes it difficult to measure absolute values of elastic strain and orientation. This limitation can be solved by using simulated EBSD patterns that are generated at known lattice states. While high fidelity simulations are expected to compare best with collected images, computational costs make it favorable to utilize a simpler model. The development of simple Bragg's Law simulations is presented as well as evidence of their utility as reference patterns.

There are simple geometric relations that connect a crystal lattice state to its projected EBSD image, but in order to represent them mathematically several reference frames must be established. The first is the crystal frame, $\hat{e}_i^{c}$, with the local crystal lattice parameters defining the basis vectors (this reference frame is typically taken to be strain free—only the rotation component of the deformation tensor is used to rotate the global reference lattice vectors to the local lattice). The second is the standard sample frame ($\hat{e}_3^{s}$ normal to the sample surface, $\hat{e}_1^{s}$ in the rolling direction, and $\hat{e}_2^{s}$ in the transverse direction). The sample frame is taken to be the external reference frame so that the rotation component of the local deformation tensor is exactly the orientation measured by traditional OIM. The third reference frame of interest is attached to the phosphor screen used to collect the EBSD images and is related to the pixilated image so that $\hat{e}_1^{v}$ points from left to right in the image (increasing columns), $\hat{e}_2^{v}$ points from top to bottom in the image (increasing rows) and $\hat{e}_3^{v}$ completes the orthonormal right-handed frame. A vector described in any of these three frames may also be rotated into another using a second rank tensor that describes a pure rotation. For example,

$$ v_i^{s} = R_{ij}^{v\rightarrow s} v_j^{v} \tag{7} $$

Now consider the Bragg's Law relationship

$$ m\lambda = 2d_{hkl}\,\sin(\theta) \tag{8} $$

This law describes two cones of angle θ that bound the diffraction band from the hkl plane for a wavelength λ. m is an integer that denotes the order of the diffraction band. Only first order ($m = 1$) diffraction bands are considered here. The deformation tensor F determines how the diffraction cones are oriented with respect to the phosphor frame and may also change the inter-planar spacing d_{hkl}. Because the equation of a cone is easiest to describe in the frame in which it is a right rectangular cone with the axis of symmetry in the z-axis, a fourth right-handed, orthonormal reference frame may be defined for convenience. Determination of a plane normal (in this case the (hkl) crystallographic plane) after deformation is a standard mechanics problem and can be found using the following equation [10]:

$$ \hat{n}' = a(\hat{n})^{T}(F)^{-1} \tag{9} $$

where $\hat{n}'$ is the normal after deformation, $\hat{n}$ is the plane normal before deformation, and a is a scalar normalization. The cone reference frame is then aligned such that $\hat{e}_3^{co} = \hat{n}'$, $0 = \hat{e}_2^{co} \cdot \hat{e}_3^{co}$, and $\hat{e}_1^{co} = \hat{e}_2^{co} \times \hat{e}_3^{co}$. In the cone reference frame, a point $\vec{p} = p_1\hat{e}_1^{co} + p_2\hat{e}_2^{co} + p_3\hat{e}_3^{co}$ lies on the cone if $p_1^2 + p_2^2 = (p_3/\tan(\theta))^2$, where the angle is the same as in Eq. (8). The CCD camera is made up of 1000×1000 pixels and each pixel can be described as a point in the cone reference frame. If a pixel falls on or between the two cones corresponding to a chosen refracting plane (hkl), then that pixel in the image of the simulated band, B, is taken to have an intensity equal to the square of the structure intensity, S_{hkl}, and zero otherwise

$$ B(\vec{p}, F, R^{v\rightarrow c}, R^{c\rightarrow co}, (hkl)) = \ldots $$
$$ \begin{cases} S_{hkl}^{2} & \text{if}([R^{c\rightarrow co}FR^{v\rightarrow c}\vec{p}]_1)^2 + ([R^{c\rightarrow co}FR^{v\rightarrow c}\vec{p}]_2)^2 \geq \left(\frac{([R^{c\rightarrow co}FR^{v\rightarrow c}\vec{p}]_3)}{\tan(\theta)}\right)^2 \\ 0 & \text{otherwise} \end{cases} \tag{10} $$

Summing the contributions of each band and its symmetry variants generates the complete approximation of the EBSD pattern image. If S^i are the elements of the symmetry subgroup and $(hkl)^{(j)}$ are the elements of the set that includes all of the diffracting planes, then the composite simulation image can be described as follows:

$$I(\vec{p},F) = \sum_i \sum_j B(\vec{p},F,S^{(i)}(hkl)^{(j)})$$

The final simulated pattern can be further filtered using high- and low-pass filters to more accurately reflect the variations in the measured EBSD pattern background.

Using the cross-correlation analysis in an iterative manner the F that minimizes the difference between a measured pattern M and a pattern simulation $I(\vec{p},F)$ is found. Because the measured pattern is a pixilated image, the simulation image must be evaluated at the locations that correspond to those pixels.

Fig. 2 shows a collected pattern from the silicon sample and a simulated pattern generated at the OIM calculated orientation. The simulated pattern had the following input parameters:

(a) diamond structure lattice, $a = 5.43$ Å
(b) 70° sample tilt angle
(c) 10° elevation angle of phosphor screen
(d) phosphor screen width $D_x = 1000$ pixels and height $D_y = 1000$ pixels
(e) pattern center (from lower left corner) $PC_x = 0.5405D_x$, $PC_y = 0.7139D_x$
(f) sample to phosphor screen distance $z^* = 0.7455D_x$
(g) orientation in Euler angles (radians): $\varphi_1 = 1.74$, $\Phi = 3.06$, $\varphi_2 = 0.11$

Furthermore, both patterns were filtered using a band pass filter. The band placement between the simulated and measured patterns aligns very well. The intensities and band widths, however, are not as precise. There are two main reasons for this. The difference in band widths is mainly due to the simulated patterns being limited to first order ($m = 1$ in Bragg's law) bands. The higher-order bands are wider and lie on the same line as the first-order bands. An example of this is the two bands intersecting at 45° angles near the center of the pattern. The presence of higher-order bands makes these appear wider than the corresponding simulated band. The difference in intensities is due to the simulations being based on a kinematical instead of a dynamical model. Dynamical models, such as those produced by Winkelmann et al. [11], account for variations in intensity in a measured pattern and in general include much more detail, but can take hours for a single pattern simulation. Since the cross-correlation method is dependent on measuring band shifts, small intensity variations and differences in band width should not affect the measurements. It is expected that continued experimentation using simulated patterns will reveal more about the issues involved with comparing kinematical simulations to measured patterns. These effects include the disregarding of dynamical diffraction and other factors such as optical distortions in the SEM column.

The patterns shown in Fig. 2 were used to test the ability of the cross-correlation function to measure shifts between measured and simulated patterns. The simulated pattern was shifted a known number of pixels and compared to the measured pattern using the cross-correlation function to measure the applied shift. This was repeated several times for increasing shifts of the simulated pattern. Fig. 3 shows the shifts applied to the simulated pattern and the corresponding measured shifts in both the horizontal and vertical directions. The cross-correlations correctly identified the shifts to within 0.05 pixels, and the standard deviation of the measured shifts from the applied shifts was 0.035 pixels. It can be seen that the spread in the measured shifts was smaller in the horizontal direction than in the vertical direction, but the exact reason for this is unknown. Deviations of a collected pattern from a simulated pattern should then be measurable to 1/20th of a pixel, which is the same level of resolution claimed by the authors of the cross-correlation method.

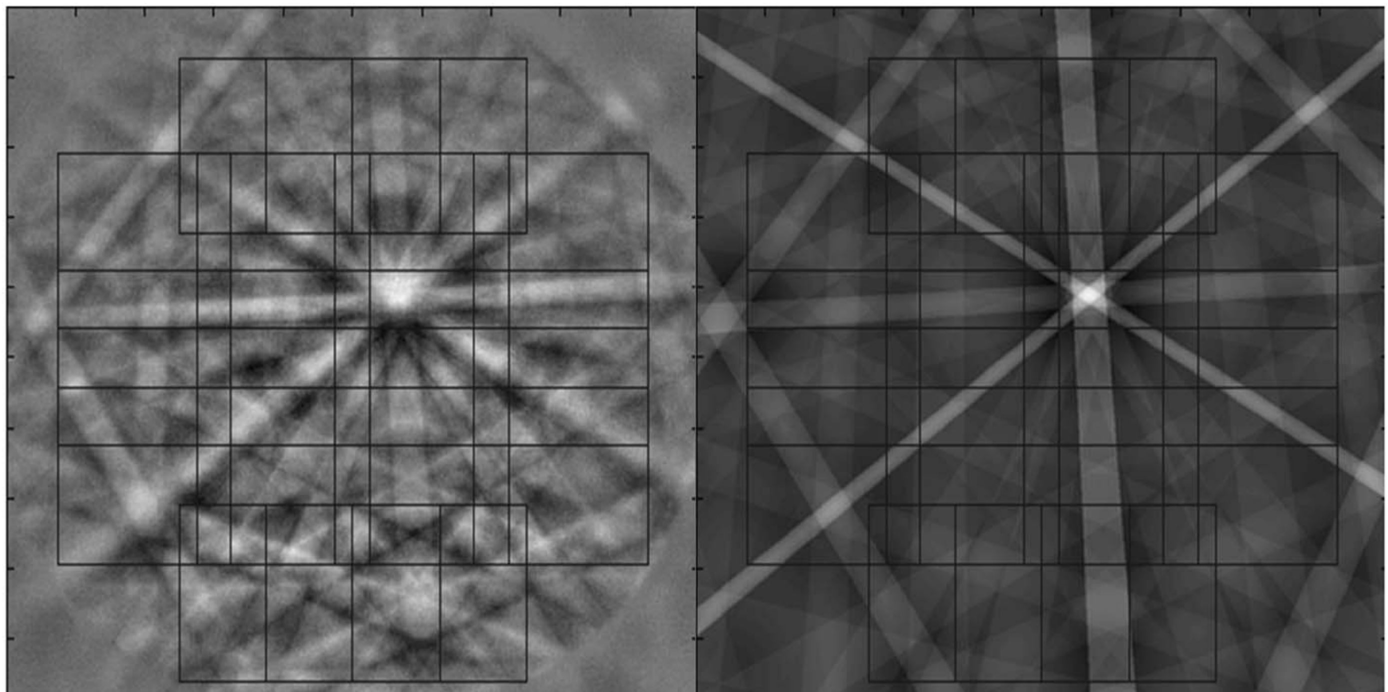

Fig. 2. Collected pattern and a simulated pattern at approximately the same orientation with outlines of ROIs drawn on.

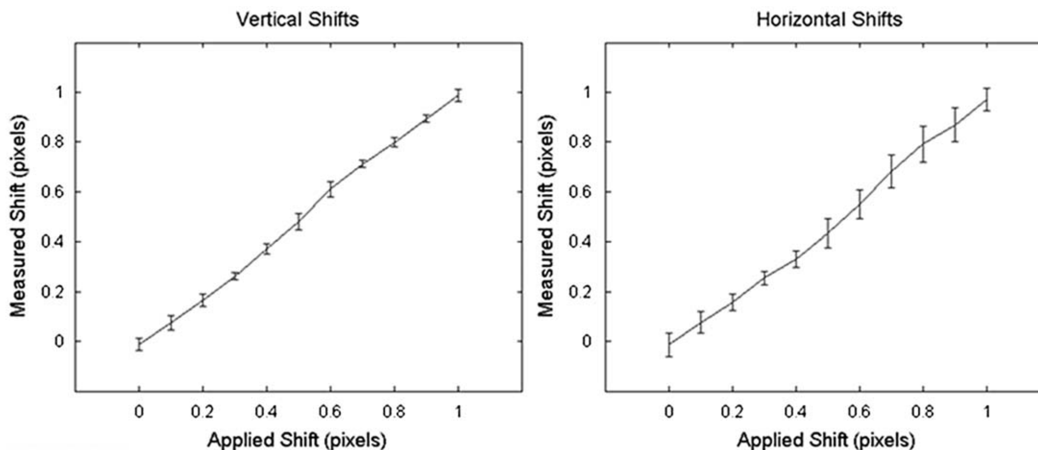

Fig. 3. Cross-correlations correctly identify shifts of a simulated image when compared to a real collected pattern. The average standard deviation of measurements was 0.035 pixels and all measured shifts in a sample of 121 different shifts lie within 0.05 pixels of the expected value.

Although the simulated patterns are visually different from collected patterns, we can conclude that they should still serve well as references for the cross-correlation analysis.

4. Strain and rotation analysis with simulated patterns

It was found during the development process of the simulated pattern method that a single comparison between a measured and simulated EBSD pattern using the cross-correlation technique did not give the desired angular and strain resolution. To improve the resolution, an iterative technique was developed using the Hough measured orientation as the starting point. The simulated pattern analysis algorithm proceeds as follows:

(1) Measure a local lattice orientation to within a 0.5° using the Hough transform method and save the EBSD pattern image.
(2) Generate a simulated pattern based on the crystal structure (which must be known) and the Hough-transform estimate of the true orientation.
(3) Use the cross-correlation analysis algorithm to compare shifts from the simulated pattern to the saved EBSD pattern image.
(4) Calculate the deformation tensor by inputting the measured shifts into Eqs. (2) and (3) and solving.
(5) Evaluate the fit of the deformation tensor with Eq. (6).

At the conclusion of these five steps, a new pattern can be simulated at a deformation state that is closer to the actual state of the examined material. If the refined simulation pattern is then used for steps 3–4, the error measure significantly improves. By repeating this process iteratively, a solution for the deformation tensor is rapidly converged upon. Additionally, the variation of the deformation tensor, calculated at each iteration, gives a concrete method of estimating the resolution of the converged solution (Fig. 4).

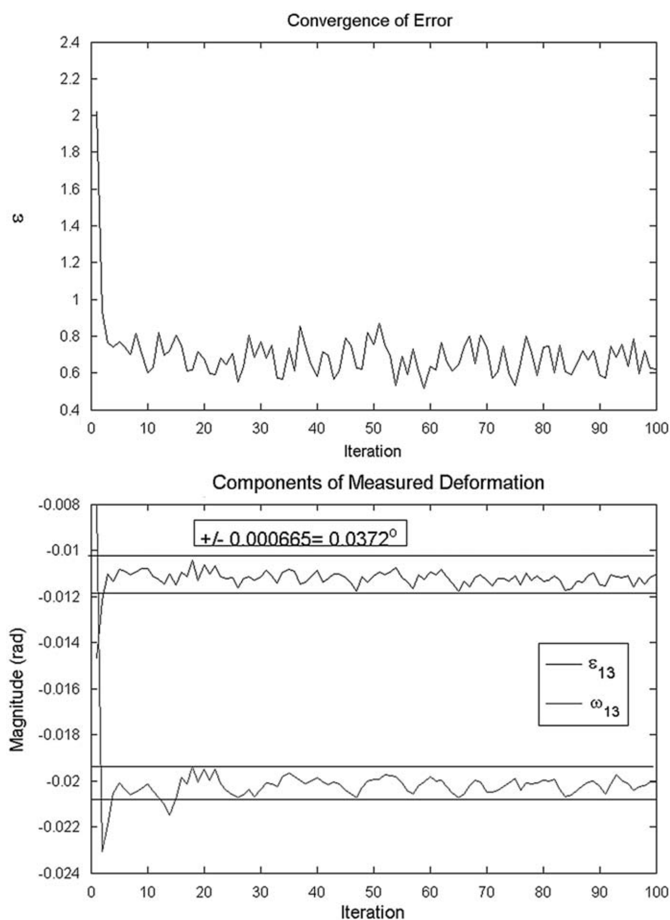

Fig. 4. As the lattice state of the simulated reference pattern is iteratively refined, measures of the error and deformation converge to a solution and provide estimates for the resolution of the solution. In this case the solution shown has a sub-pixel resolution (top), which corresponds to a resolution of 0.0372° for individual components of the rotation tensor and 0.000665 for components of the strain tensor (bottom).

Due to the difficulty of establishing an absolute external measure of the resolution for these new techniques, Wilkinson devised a test for inferring the resolution limits. He applied a known rotation manually to a sample in the microscope chamber and then collected five patterns at each increment of rotation. The rotation control of the stage does not have sufficient precision to adequately probe the resolution of this method, so instead he took the standard deviation of the five measurements at a constant angle of rotation to be the resolution limit. This procedure was repeated using a single crystal [0 0 1] silicon sample with the modified Wilkinson analysis, and then with the simulated pattern analysis (Fig. 5).

The Wilkinson cross-correlation method provided an average standard deviation of 0.003° for rotation components and 5.5×10^{-5} for strain components when using the standard deviation of the measurement of five collected patterns at the

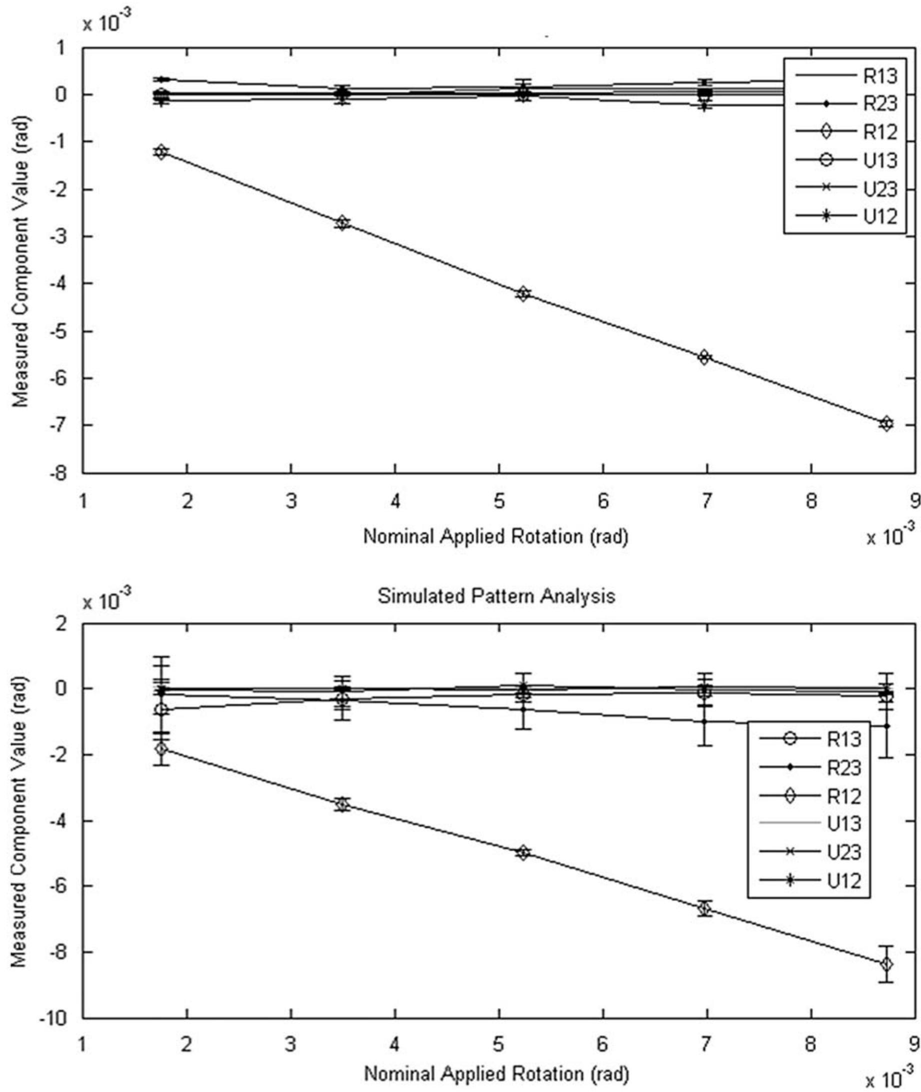

Fig. 5. Using manual stage rotations the resolution of the modified Wilkinson method (top) can be compared to the simulated pattern method (bottom). Since the normal to the stage is the $\hat{e}_3$ axis, the R_{12} component of the rotation tensor should be the only non-zero component. The reader is reminded that U is the elastic strain gradient tensor.

same orientation, which agrees with the measurements reported by Wilkinson (0.006° and 1×10^{-4}). The simulated pattern analysis method had slightly poorer resolution with an average standard deviation of 0.02° and 3.6×10^{-4} for rotation and strain components, respectively.

An important issue not addressed by the rotation test is the simulated pattern method's sensitivity to input simulation parameters. These parameters include the pattern center, sample to phosphor screen distance, sample tilt, accelerating voltage, and the material lattice parameters. In order to study how error in input lattice parameters could affect the accuracy of the simulated pattern method, simulated patterns were compared using the cross-correlation method. Two patterns were simulated at the exactly same lattice state. The only difference between the two were differences in the input x and y coordinates of the pattern center and the sample to screen distance. Fig. 6 shows how these small changes translate to error in elastic strain measurements. In general, pattern center and sample to screen distance can be found using OIM software to $\sim0.005D_x$.

While the error caused by variations in the pattern center are generally below the resolution limit of the simulated pattern method, error in the sample to screen distance can have a

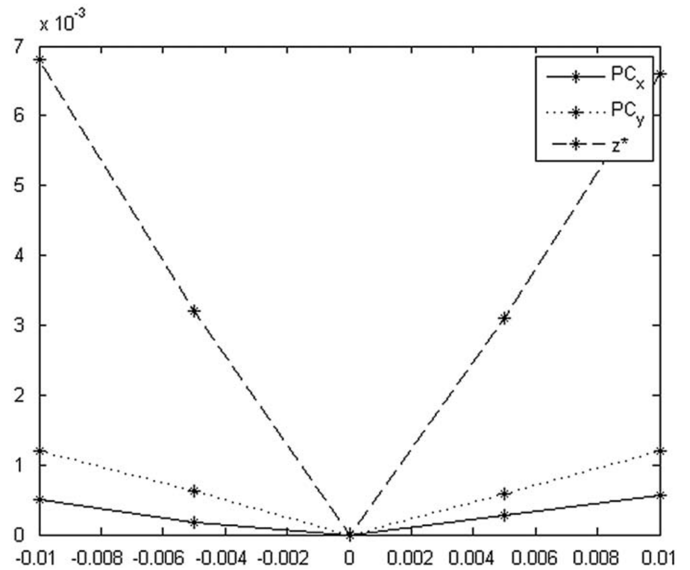

Fig. 6. Average elastic strain measurements resulting from a difference in input pattern center and sample-to-screen distance. The patterns were simulated at zero elastic strain.

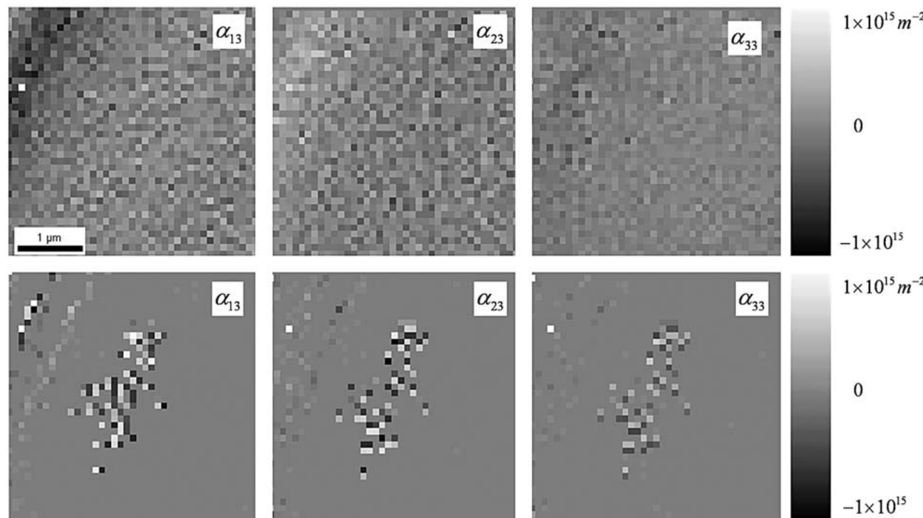

Fig. 7. Spatial distribution of the α_{13}, α_{23}, and α_{33} components of the dislocation density tensor as estimated by the simulated pattern method (top row) compared to the estimation made using conventional OIM data (bottom row). Notice the sensitivity to fine-scale detail of the simulated pattern method shown by the gradient towards higher dislocation density in the upper left corner. The OIM data shows some detail, but is mostly dominated by noise.

significant effect on the accuracy of results. To address this issue, a method is currently being developed to carry out high-resolution sample to screen distance calibration using single crystals mounted planar with the sample in the SEM chamber (Fig. 7).

Although the resolution of the simulated pattern reference method at this stage of development does not achieve that of Wilkinson's method, the iterative simulation approach has distinct advantages that make it worth pursuing. First, by comparing a simulated pattern to a collected pattern, any pattern defects are limited to one pattern and the impact of image quality and need for user-controlled filtering is significantly decreased. Second, using a pattern of known character allows calculation of absolute strain and rotation without special requirements of the sample, whereas in the Wilkinson method this would require a strain-free portion of the sample to use as a reference. Additionally, this means that the method of simulated references could easily analyze a polycrystalline sample, whereas for the collected pattern reference method, each new grain would require a new strain-free reference pattern, which may be especially difficult in small or highly deformed grains.

5. Results: dislocation density measurements in MG AZ91

Dislocation density measurements are an important factor in the development of new metallic materials. Due to its light weight and high recyclability, magnesium alloys are very attractive prospects for applications in car parts. However, their use is limited by low ductility and formability at low temperatures. This low ductility is based on the low number of slip systems that are active at room temperatures. One way to see this effect is through studying the dislocation densities caused by slip in the crystal lattice. A better understanding of the dislocation structure can lead to a more fundamental understanding of the deformation mechanisms of magnesium.

Strain and orientation measurements obtained using the simulated pattern method were used to estimate the geometrically necessary dislocation (GND) density in a polycrystalline Mg-based AZ91 alloy. Continuum mechanics-based derivations of GND densities have been founded on the original work of Nye [12] and later with the addition of elastic strain by Kröner [13]. The following formula emerged, linking lattice curvature (κ_{ij}), which is the curl of the orientation field, and elastic strain gradients ($\varepsilon_{ij,l}$) to the dislocation density tensor (α_{ij}):

$$\alpha_{ik} = \kappa_{ki} - \delta_{ki}\kappa_{pp} + e_{klj}\varepsilon^{e}_{ij,l} \tag{11}$$

The components of the dislocation density tensor weight the dyadic formed by the direction of the dislocation line and the Burgers vector characterizing that dislocation. The tensor can be calculated using a point by point comparison of elastic strain and orientation information obtained using EBSD-based techniques [14,15]. The effect of any statistically stored dislocations between steps that have opposite signs (Burgers vectors in opposite directions) will cancel out, and thus will be immeasurable by the proposed technique. In order to get the most accurate estimate of the actual dislocation density, it is vital to use as small a step size as possible when making orientation and strain measurements. However, as smaller step size lengths are approached, any errors from misorientation measurements are significantly amplified in the curvature measurements, and artificially high dislocation densities can be measured. OIM is limited by a misorientation resolution of approximately 0.5°, which corresponds to a dislocation density measurement resolution of $\sim 3 \times 10^{15}\,\text{m}^{-2}$. The simulated pattern method's improved resolution has allowed dislocation densities of the order of $1 \times 10^{13}\,\text{m}^{-2}$ to be measured in single crystal samples.

The simulated pattern method was applied to a polycrystalline Mg AZ91 sample that had been compressed 5.5%. The normal to the sample surface was parallel to the compression direction. The sample was prepared and scanned at GM facilities in Detroit. A $4 \times 4\,\mu\text{m}^2$ scan was taken near the center of a $20 \times 20\,\mu\text{m}^2$ grain at a 100 nm step size. The scan was taken using an accelerating voltage of 20 kV and at a working distance of 12 mm. In order to obtain the highest signal-to-noise ratio possible, the EBSD patterns were saved at the full camera resolution which slowed scanning time to $\sim$3 patterns/s. To further improve the accuracy of the cross-correlations, a band pass filter was used on the overall patterns (both measured and simulated). Also, to further improve the ability of the cross-correlation function to detect bands, each individual ROI was filtered using a low-pass filter. The cut-off frequencies for the band pass filters (in cycles per pixel) were 0.65

Table 1
Comparison of methods.

	OIM	Simulated pattern method without elastic strain term	Simulated pattern method with elastic strain term	Wilkinson method with elastic strain term
α_{13}	3.94e15	9.12e13	1.18e14	1.53e14
α_{23}	2.94e15	1.25e14	1.60e14	1.16e14
α_{33}	1.81e15	9.12e13	7.70e13	1.08e14
α_{total}	8.70e15	3.08e14	3.55e14	3.76e14

Dislocation density measurements in m^{-2} using OIM, the simulated pattern method, and Wilkinson's method with and without including the elastic strain term.

for the high pass and 32.3 for the low pass. The cut-off frequency of the low-pass filter was 0.77 cycles per pixel. These values were obtained by visual optimization to minimize the scatter in the data. The authors intend to conduct a thorough study of the filtering effects on the results, but such a study has not yet been carried out at this time. The saved patterns were analyzed offline using the simulated pattern method with the OIM measured orientation as the starting point in the iterations. The offline analysis time is dependent on the number of iterations used, which is generally 3–5. For 465×465 pixel images, each iteration requires $\sim$0.5 s, with two-thirds of the time used for pattern simulation and the rest to perform the cross-correlation analysis. The code used has not been optimized for speed, and it is expected that the time requirements will be significantly reduced in the future.

The dislocation density was first estimated using the OIM measured orientation, then using the simulated pattern method with and without including the elastic strain term, and finally using the simulated pattern method measured orientation and elastic strain at each point. Since dislocation density measurements need only the gradients of the elastic strain and orientation, Wilkinson's method was also used as a comparison to further validate the simulated pattern method. The dislocation density was defined as the average of the absolute magnitude of all of the points in the scan (Table 1).

The data obtained using Wilkinson's method was very close to that obtained using the simulated pattern method. This serves as further validation of the accuracy of the results. The OIM estimated dislocation density on the other hand was over a full order of magnitude higher than that estimated using the simulated pattern method. In general, OIM is incapable of measuring dislocation densities below $\sim 3 \times 10^{15}\ m^{-2}$, so the estimated density in this case is around what would be expected if only noise was measured. Although no significant structure is seen in the figure, there are two important points to be taken from it. First, the dislocation density measurements using the simulated pattern method are over a full order of magnitude lower than those measured by traditional OIM. This is directly related to the increase in angular resolution of the simulated pattern method. Second, the dislocation density maps created by traditional OIM have many very high points as can be seen in the center of the scan, while other points show a very low dislocation density. These sharp changes in dislocation density are attributed to scatter in the orientation data collected by OIM and suggest that while the overall dislocation density measured by OIM may differ from the simulated pattern method by only an order of magnitude, local variations caused by scatter can cause much higher levels of error.

From the data, it is also seen that the elastic strain term can have a significant effect on the estimated dislocation density. Depending on how the elastic strain aligns with the dislocations, the inclusion of the elastic strain tensor can cause a higher or lower dislocation density to be estimated. In this case, the overall estimated dislocation density increased 15% after the inclusion of the elastic strain term.

6. Conclusion

Initial studies of simple Bragg's Law simulation patterns as references for cross-correlation analysis of EBSD data show resolution limits above traditional OIM techniques and approaching the limits of the high-resolution cross-correlation technique of Wilkinson. Most importantly, the simulated pattern method eliminates the need for a strain-free reference pattern, allowing the characterization of polycrystalline materials and other materials where a strain-free reference pattern may not be available. Although the algorithms used for this study were significantly slower than traditional analysis, they were easily performed offline in an automated manner.

There are a currently a number of experimental analyses being developed to showcase the capabilities of this simulated pattern method. One application that is currently being explored is phase differentiation in steel samples. The bainite and martensite phases in steels have a tetragonality in their lattices caused by carbon content that distinguish them from the cubic ferrite phase. Currently, there is no agreement found in the literature on the tetragonality in the crystal lattice of the bainite phase [16]. The magnitude of this tetragonality is too small for traditional EBSD techniques to directly detect but should, however, be detectable in the diagonal components of the elastic strain tensor when found using the simulated pattern method. The axis of tetragonality can also be found by simulating EBSD patterns with tetragonalities along each of the three axis, comparing them to measured patterns from bainite or martensite phases, and finding which axis of tetragonality fits best with the measured pattern. Pseudo-symmetries in phases that are slightly altered from standard lattices should also be accessible. Another example that has previously been investigated and has been revisited in this paper is the use of the improved resolution limits to determine dislocation densities [14]. While Wilkinson's method is perhaps superior for measuring dislocation densities in materials with small deformations, large deformations can cause high orientation gradients that can lead to significant errors when using Wilkinson's approach. As improvements are made to the algorithm and computational approaches, using Bragg's Law simulation patterns as references for cross-correlation analysis will only become more useful and feasible.

Acknowledgments

The authors wish to acknowledge funding from the Army Research Office, Dr. David Stepp Program Director. Collaboration with Dr. Raj Mishra of GM Research is also gratefully acknowledged.

References

[1] B.L. Adams, S.I. Wright, K. Kunze, Orientation imaging: the emergence of a new microscopy, Metallurgical Transactions A (Physical Metallurgy and Materials Science) 24A (4) (1993) 819–831.
[2] S.I. Wright, Review of automated orientation imaging microscopy (OIM), Journal of Computer-Assisted Microscopy 5 (207) (1993).

[3] K.Z. Troost, P. Sluis, D.J. Gravesteijn, Elastic strain determination by backscatter Kikuchi diffraction in the scanning electron microscope, Applied Physics Letters 62 (10) (1993) 1110–1112.
[4] A.J. Wilkinson, G. Meaden, D.J. Dingley, High resolution mapping of strains and rotations using electron back scatter diffraction, Materials Science and Technology 22 (11) (2006) 1–11.
[5] A.J. Wilkinson, G. Meaden, D.J. Dingley, High-resolution elastic strain measurement from electron backscatter diffraction patterns: new levels of sensitivity, Ultramicroscopy 106 (2006) 307–313.
[6] X. Tao, A. Eades, Monte Carlo simulation for electron backscattering diffraction, Microscopy and Microanalysis 10 (2) (2004) 940–941.
[7] J.P. Lewis, Fast template matching, Vision Interface (1995) 120–123.
[8] X. Tao, A. Eades, Measurement and mapping of small changes of crystal orientation by electron backscattering diffraction, Microscopy and Microanalysis 11 (2005) 341–353.
[9] X. Tao, A. Eades, Errors, artifacts, and improvements in EBSD processing and mapping, Microscopy and Microanalysis 11 (2005) 79–87.
[10] A.J.M. Spencer, in: Continuum Mechanics, Longman, New York, 1980.
[11] A. Winkelmann, et al., Many-beam dynamical simulation of electron backscatter diffraction patterns, Ultramicroscopy 107 (2007) 414–421.
[12] J.F. Nye, Some geometrical relations in dislocated crystals, Acta Metallurgica 1 (1953) 153–162.
[13] E. Kroner, Continuum theory of dislocations and self-stresses, Ergebnisse der Angewandten Mathematik 5 (1958) 1327–1347.
[14] S. Sun, B.L. Adams, W.E. King, Observations of lattice curvature near the interface of a deformed aluminium bicrystal, Philosophical Magazine A: Physics of Condensed Matter, Structure, Defects and Mechanical Properties 80 (1) (2000) 9–25.
[15] C. Landon, B. Adams, J. Kacher, High resolution methods for characterizing mesoscale dislocation structures, Journal of Engineering Materials and Technology 130 (2) (2008) 40–45.
[16] M.X. Zhang, P.M. Kelly, Determination of carbon content in bainitic ferrite and carbon distribution in austenite by using CBKLDP, Materials Characterization 40 (1998) 159–168.